The Astrophysical Journal Supplement Series, 229:2 (16pp), 2017 March https://doi.org/10.3847/1538-4365/229/1/2

The Second Flight of the SUNRISE Balloon-borne Solar Observatory: Overview of Instrument Updates, the Flight, the Data, and First Results

S. K. Solanki[1,2], T. L. Riethmüller[1], P. Barthol[1], S. Danilovic[1], W. Deutsch[1], H.-P. Doerr[1,3], A. Feller[1], A. Gandorfer[1], D. Germerott[1], L. Gizon[1,4], B. Grauf[1], K. Heerlein[1], J. Hirzberger[1], M. Kolleck[1], A. Lagg[1], R. Meller[1], G. Tomasch[1], M. van Noort[1], J. Blanco Rodríguez[5], J. L. Gasent Blesa[5], M. Balaguer Jiménez[6], J. C. Del Toro Iniesta[6], A. C. López Jiménez[6], D. Orozco Suarez[6], T. Berkefeld[3], C. Halbgewachs[3], W. Schmidt[3], A. Álvarez-Herrero[7], L. Sabau-Graziati[7], I. Pérez Grande[8], V. Martínez Pillet[9], G. Card[10], R. Centeno[10], M. Knölker[10], and A. Lecinski[10]

[1] Max Planck Institute for Solar System Research, Justus-von-Liebig-Weg 3, D-37077 Göttingen, Germany; solanki@mps.mpg.de
[2] School of Space Research, Kyung Hee University, Yongin, Gyeonggi, 446-701, Korea
[3] Kiepenheuer-Institut für Sonnenphysik, Schöneckstr. 6, D-79104 Freiburg, Germany
[4] Institut für Astrophysik, Georg-August-Universität Göttingen, Friedrich-Hund-Platz 1, D-37077 Göttingen, Germany
[5] Grupo de Astronomía y Ciencias del Espacio, Universidad de Valencia, E-46980 Paterna, Valencia, Spain
[6] Instituto de Astrofísica de Andalucía (CSIC), Apartado de Correos 3004, E-18080 Granada, Spain
[7] Instituto Nacional de Técnica Aeroespacial, Carretera de Ajalvir, km 4, E-28850 Torrejón de Ardoz, Spain
[8] Universidad Politécnica de Madrid, IDR/UPM, Plaza Cardenal Cisneros 3, E-28040 Madrid, Spain
[9] National Solar Observatory, 3665 Discovery Drive, Boulder, CO 80303, USA
[10] High Altitude Observatory, National Center for Atmospheric Research, P.O. Box 3000, Boulder, CO 80307-3000, USA
Received 2016 July 20; revised 2017 January 5; accepted 2017 January 5; published 2017 March 22

Abstract

The SUNRISE balloon-borne solar observatory, consisting of a 1 m aperture telescope that provides a stabilized image to a UV filter imager and an imaging vector polarimeter, carried out its second science flight in 2013 June. It provided observations of parts of active regions at high spatial resolution, including the first high-resolution images in the Mg II k line. The obtained data are of very high quality, with the best UV images reaching the diffraction limit of the telescope at 3000 Å after Multi-Frame Blind Deconvolution reconstruction accounting for phase-diversity information. Here a brief update is given of the instruments and the data reduction techniques, which includes an inversion of the polarimetric data. Mainly those aspects that evolved compared with the first flight are described. A tabular overview of the observations is given. In addition, an example time series of a part of the emerging active region NOAA AR 11768 observed relatively close to disk center is described and discussed in some detail. The observations cover the pores in the trailing polarity of the active region, as well as the polarity inversion line where flux emergence was ongoing and a small flare-like brightening occurred in the course of the time series. The pores are found to contain magnetic field strengths ranging up to 2500 G, and while large pores are clearly darker and cooler than the quiet Sun in all layers of the photosphere, the temperature and brightness of small pores approach or even exceed those of the quiet Sun in the upper photosphere.

Key words: Sun: chromosphere – Sun: faculae, plages – Sun: magnetic fields – Sun: photosphere – sunspots – techniques: polarimetric

Supporting material: animation

1. Introduction

Probing the Sun at high resolution has time and again revealed new phenomena not previously seen. Examples are the discovery of umbral dots by Beckers & Schröter (1968), facular bright points by Mehltretter (1974), dark cores in penumbral filaments by Scharmer et al. (2002), lateral downflows in penumbral filaments by Joshi et al. (2011a, 2011b), Scharmer et al. (2011), or the ultrafine loops reported by Ji et al. (2012).

In spite of the significant advances made by ground-based observations, it remains challenging to accurately take into account or fully remove the effects of atmospheric seeing from observational data. In addition, high-resolution studies from the ground are generally limited to wavelengths with high photon flux and usually to short periods of stable seeing. Thus, in spite of having an aperture smaller than that of the largest ground-based telescopes, the space-based Solar Optical Telescope onboard *Hinode* (Tsuneta et al. 2008) has resulted in many advances. These include the discovery of penumbral microjets (Katsukawa et al. 2007), waves carrying copious amounts of energy along spicules (De Pontieu et al. 2007), ubiquitous linear-polarization signals in the quiet Sun (Orozco Suárez et al. 2007; Lites et al. 2008; Lagg et al. 2016), or very fast downflows at the ends of particular penumbral filaments (van Noort et al. 2013). Hence, an even larger solar telescope located above the bulk of the Earth's atmosphere has an extensive discovery space.

The largest solar telescope (along with the Soviet Stratospheric Solar Observatory; Krat et al. 1974) to have reached the near-space conditions of the stratosphere is SUNRISE, which had a very successful first flight in 2009 June (for an overview of earlier balloon-borne solar telescopes and results see Solanki et al. 2010). The data obtained during that first flight of SUNRISE have led to the following discoveries and insights, among many other results.

1. First ever spatially resolved images of small-scale intense magnetic flux concentrations in the quiet Sun show that semi-empirical flux tube models provide a reasonable description of such structures (Lagg et al. 2010).

2. First ever brightness measurements of flux concentrations in the UV at 312, 300 and 214 nm reveal very high intensities, up to a factor of 5 above the mean quiet-Sun brightness at 214 nm (Riethmüller et al. 2010).
3. First ever measurements of the rms intensity contrast of granulation in the UV show high values of up to 30%, consistent with numerical simulations. These values provide a direct measure of the efficiency of convective energy transport by granulation (Hirzberger et al. 2010).
4. The most sensitive high-resolution time sequences of maps of the vector magnetic field ever obtained reveal abundant, short-lived and highly dynamic small-scale horizontal fields (Danilovic et al. 2010).
5. Ubiquitous small-scale whirl flows are found which drag small-scale magnetic field structures into their centers (Bonet et al. 2010).
6. Magnetic field extrapolations from SUNRISE/IMaX data indicate that most magnetic loops in the quiet Sun remain within the photosphere. Only a small fraction reaches the chromosphere. Most of these higher-lying loops are anchored (at least in one foot point) in the strong-field elements of the network (Wiegelmann et al. 2010).
7. Discovery of large amplitude acoustic waves in the quiet solar atmosphere. Such waves were missed in the past, since they are spatially strongly localized and their photospheric sources move significantly within a short time (Bello González et al. 2010).
8. First detection of horizontally oriented vortex tubes in solar convective features. Such vortex tubes were found to be rather common in solar granules (Steiner et al. 2010).
9. Discovery that the internetwork magnetic elements continuously move back and forth between a state of weak and strong magnetic field (Martínez González et al. 2011; Requerey et al. 2014).
10. First determination of the inclination of magnetic elements directly from their position in images sampling different heights. The results reveal that the magnetic elements are nearly vertical, in contrast to inversion techniques that suggested that they were close to horizontal (but in this case were strongly affected by noise; Jafarzadeh et al. 2014).
11. First detection of localized, strongly wavelength-shifted polarization signals in the quiet Sun that are interpreted as supersonic upflows caused by magnetic reconnection of emerging small-scale loops with pre-existing fields (Borrero et al. 2010), confirmed by *Hinode* observations (Martínez Pillet et al. 2011b).
12. Discovery that 85% of the internetwork magnetic fields stronger than 100 G are concentrated in mesogranular lanes, although there is no particular mesogranular scale (Yelles Chaouche et al. 2011).

The data taken during the first flight of the SUNRISE observatory were limited to the quiet Sun, as the Sun was exceedingly quiet for the whole duration of the flight. To be able to probe an active region with the unique capabilities of the SUNRISE observatory, a reflight of the largely (but not completely) unchanged instrumentation was carried out in 2013 June. In this paper we describe the updates of the instruments and of the data reduction. We also provide an overview of the obtained data and of the first results obtained from this second flight of SUNRISE. A set of results from this second flight are described in the publications that are part of this special issue (which also contains some papers making use of data from the first SUNRISE science flight).

In the following we shall often refer to the instrumentation as flown during the first flight in 2009 and the corresponding mission as SUNRISE I, while the updated instrumentation flown in 2013 and that flight are referred to as SUNRISE II.

The paper is structured as follows. In Section 2 we provide a summary of the updates to the instrumentation, concentrating mainly on changes made relative to the first flight in 2009. In Section 3, the 2013 flight is described and an overview of the obtained data is given in Section 4. The updated data reduction procedures are described in Section 5, again focusing on the parts that changed relative to the first flight. Some snapshots of the reduced data are discussed in Section 6. Finally, conclusions and an outlook on future plans for SUNRISE are presented in Section 7.

2. Instrumentation Update

SUNRISE II is composed of a Gregory telescope with a main mirror of 1 m diameter and two post-focus instruments located above it, together with the Image Stabilization and Light Distribution unit (ISLiD) and the Correlating Wavefront Sensor (CWS). The telescope and instruments are mounted in a gondola hanging under a zero-pressure balloon. The system is stabilized by the gondola and a tip-tilt mirror located in ISLiD that is controlled by the CWS. The post-focus instruments are the SUNRISE Filter Imager (SuFI), that observes in five wavelength channels between roughly 2000 and 4000 Å, and a filter magnetograph, the Imaging Magnetograph eXperiment (IMaX), observing in the Fe I 5250.2 Å spectral line, a Zeeman triplet with a Landé factor of $g = 3$. The complete instrumentation is described in brief by Solanki et al. (2010) and in greater detail by Barthol et al. (2011). Further information on ISLiD and on SuFI is given by Gandorfer et al. (2011), IMaX is described by Martínez Pillet et al. (2011a), and more information on the CWS is provided by Berkefeld et al. (2011).

The major components of SUNRISE I, such as the gondola, the telescope and the post-focus instrumentation (PFI) suffered only minor damage during the landing after the first science flight in 2009 and could be reworked and prepared for a reflight with comparatively little effort. Below we describe the main changes to the hardware that were made in preparation for the second flight.

2.1. Gondola, Telemetry, and Telescope

Gondola. Structural protective elements on the gondola, such as the crush pad assembly below the core gondola frame or the front and rear roll cages, needed to be replaced, as they were designed to deform and thus to take most of the impact energy to protect the rest of the payload. In addition to such refurbishment, modifications were implemented to the gondola, as described below.

The average power consumption during the first flight was much lower than previously estimated, so that the number of solar cells could be reduced to only six panels with 80 SunPower A-300 cells each (from originally 10 panels in 2009). The panels were mechanically re-arranged, reducing the overall width of the instrument. This modification allowed a pre-installation of the solar panels in the integration hall before roll-out, saving precious time on the day of the launch.

Additional benefits are reduced mass and a lower aerodynamic cross section.

The mounting of the electronics racks, carrying all the instrument computers, pointing system computer and power distribution units, was modified for the 2013 flight. Instead of having a 20° tilt toward cold sky as in the previous configuration, the racks were now mounted vertically and were directly attached to the gondola side trusses, providing higher overall stiffness and reduced mass. The reduction in thermal efficiency of this configuration was seen to be acceptable, as results from the 2009 flight indicated that the size of the radiating surfaces are sufficiently large to dump all dissipated heat at moderate temperatures even in this slightly less efficient configuration.

As part of the on-ground testing before the flight, a modal survey test was performed to determine the first natural eigenmodes of the complete instrument. A set of externally mounted accelerometers recorded the impulse and frequency response to an impact on the gondola structure. It was verified that the 10 Hz oscillation observed in the pointing data of the 2009 science flight corresponds to the first torsional bending mode of the gondola core framework. Modifications of software filters were then implemented into the pointing system control loops, preventing excitation of this mode during the 2013 flight. Pointing system housekeeping data taken during the 2013 flight clearly demonstrated their efficiency, as almost no 10 Hz oscillations were present during the time spent at float altitude and in particular not when pointing at the Sun.

Telemetry. The 2009 flight operations and commissioning were hampered by the early loss of the E-Link high-speed telemetry provided by ESRANGE,[11] which ceased operation after only a few hours when switching from one ground station to another. For the rest of the 2009 mission commanding and health status information was transmitted through a 6 kbit s^{-1} TDRSS link, where TDRSS is the Tracking and Data Relay Satellite System, a NASA network of communication satellites on geosynchronous orbits and associated ground stations used for space-to-ground communication. This was found to be clearly insufficient.

In preparation for the 2013 science flight the SUNRISE team helped to qualify the Iridium Pilot/OpenPort system for balloon flights. A dedicated test set-up was flown on 2011 September 28 and October 7 from Ft. Sumner on balloons of the Columbia Scientific Ballooning Facility (CSBF) of NASA for several hours each, to verify system integrity during launch, ascent, and operational conditions. The bandwidth transmitted to ground was more than ten times higher than with the TDRSS Omni link. SUNRISE II was one of the first scientific missions to be supported with this new telemetry system. The antenna system on top of the gondola was re-arranged to provide the required 6 ft clearance to the dome-shaped Iridium transmitter. SUNRISE II reached an average data rate of 100 kbit s^{-1}, and downlink of science data continued even after the payload landed, although the antenna was partly buried in Canadian soil.

Telescope and structure. The telescope and instrumentation needed a thorough cleaning and refurbishment. All mechanisms were disassembled, inspected, cleaned, lubricated, re-assembled, and requalified. The motor and gears of the telescope aperture mechanism were replaced and the mechanism was improved to provide a more reliable detection of the open or closed position. Key elements of the carbon-fiber based structure were inspected, strength tested, and found to be still fully intact. The thermal subsystem consisting of the heat rejection wedge and its radiators needed to be refurbished. New second surface mirrors were attached. All telescope mirror coatings were stripped, the mirrors cleaned, their optical quality interferometrically verified and recoated. The secondary mirror needed to be replaced completely, as the Zerodur mirror substrate was damaged during the landing and recovery after the 2009 flight. The mirror was refabricated by the Lytkarino Optical Glass Factory in Moscow, with a performance identical to the original one.

The telescope alignment proved to be a challenge, because a sufficiently large reference flat mirror provided by SAGEM for the 2009 flight was not available this time. Since on the launch site a misalignment of the telescope was detected (the telescope had been tested before departure to Kiruna without a 1 m reference flat, making the performance assessment ambiguous), a readjustment of the M2 position was necessary.

Figure 1 shows two views of the SUNRISE II payload (telescope with instruments and electronics mounted in the gondola) hanging from the launch crane at the ESRANGE balloon launch facility. More details about the whole system are provided by Barthol et al. (2011).

2.2. Post-focus Instrumentation

The instrumentation mounted within the PFI platform survived the landing and recovery in good shape. Some cleaning was necessary, but almost all elements could be reused. The PFI was refurbished, but remained technically identical to the one used during the 2009 flight. The scientific instruments were also refurbished and subsequently integrated and realigned.

ISLiD. The ISLiD system (Gandorfer et al. 2011) was not modified relative to the first flight. In order to optimize the end-to-end optical performance of the combined ISLiD–IMaX path, an additional plane-parallel plate was introduced into the converging IMaX feed path in front of the IMaX interface focus. By choosing the inclination and orientation of this plate, residual astigmatism in the ISLiD/IMaX path could be minimized. The plate was coated with high-efficiency anti-reflective layers on both sides, which were tuned to be unpolarizing at the selected angle of incidence.

CWS. The main improvement to the CWS (Berkefeld et al. 2011) for the 2013 flight consisted of a second operating mode. By reading out only the two sub-apertures in the center row (marked red in Figure 2), the bandwidth could be substantially increased and the residual image jitter decreased. Table 1 compares the two modes.

Due to the better performance, the two-sub-aperture mode was used exclusively during the 2013 flight. Further software improvements included better data logging capabilities and much faster focusing after closing the CWS control loop.

SuFI. The SuFI (Gandorfer et al. 2011) was changed very little compared to the SUNRISE I flight. Thus, the mechanical shutter, which had seen more than 150,000 releases during the 2009 flight, was replaced. For the SuFI CCD camera a new power supply unit with very low output noise was developed.

[11] The ESRANGE Space Center (67.89°N, 21.10°E) near Kiruna, northern Sweden is a European research center and launch facility for sounding rockets and balloons that is managed by the Swedish Space Corporation. ESRANGE is financed by the Esrange Andøya Special Project (EASP) within ESA (European Space Agency). The member states of ESA/EASP today are France, Germany, Switzerland, Norway, and Sweden.

(a)

(b)

Figure 1. Two views of the flight-ready SUNRISE II payload prior to the 2013 flight hanging from the launch crane at ESRANGE. Image (a) shows the payload during the electromagnetic compatibility test. The telescope front-ring can be seen along with the radiators mounted above it. Multi-layer insulation (MLI) is used to thermally insulate the telescope and the instruments. Image (b) shows more clearly the gondola structure, including front and rear roll cages.

This led to an improvement in signal-to-noise performance by a factor of more than ten. In addition, three of the wavelength filters were exchanged. The filter set for observations in the 2140 Å region was replaced by a combination of two different filters, both of which had a FWHM of 210 Å, but had different side band characteristics, which ensured sufficient blocking of longer wavelength radiation. The 3120 Å channel of SUNRISE I was replaced by a combination of a 2795 Å filter with 4.8 Å width and two blockers of 300 Å and 110 Å width, respectively. This combination of filters, whose profile is plotted in Figure 1 of Riethmüller et al. (2013a), is centered on the Mg II k line and gets minimal contribution from the Mg II h line located in the filter profile's wings. Observations in the Ca II H line were possible through two different filters centered at 3968 Å. In addition to the 1.8 Å wide filter already used in SUNRISE I, a 1.1 Å wide filter was available, which provided better isolation of the contributions from higher atmospheric

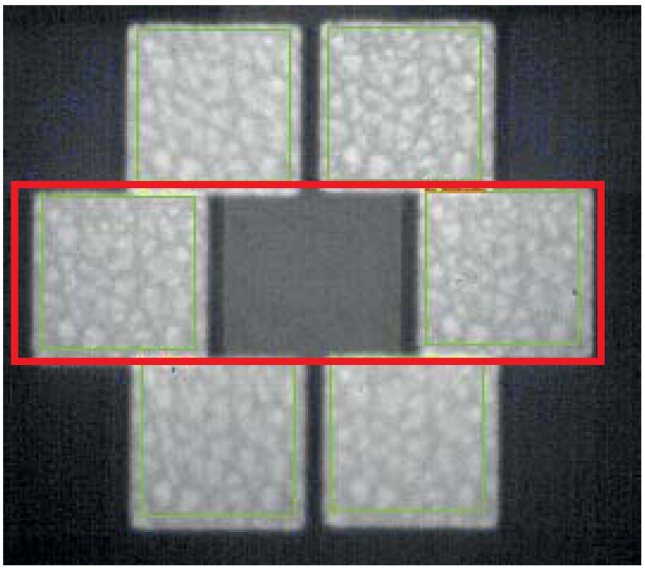

Figure 2. Snapshot of the image recorded by the Correlating Wavefront Sensor (CWS), showing the six sub-apertures displaying the same solar scene. The red frame bounds the two images employed in the two-sub-aperture mode.

Table 1
CWS Parameters for the Six-sub-aperture and Two-sub-aperture Modes

Parameter	6-sub-aperture mode	2-sub-aperture mode
Control loop frequency (Hz)	1400	4000
Bandwidth (0db) (Hz)	90	140
Measurement accuracy (mas)	2	4
Detectable Zernike modes	tilt, focus, coma	tilt, focus
Residual image jitter [mas rms]	50 (in 2009) 35 (in 2013)	⋯ 25 (in 2013)

layers. In the following, these channels are referred to as the 3968w ("w" for wide wavelength band) and 3968n ("n" for narrow band) channels. The 3880 Å channel, which was used in SUNRISE I, was sacrificed for this purpose.

IMaX. The IMaX (Martínez Pillet et al. 2011a) on the 2013 flight was also very similar to the version flown on SUNRISE I, although a number of smaller changes and updates had been made. The parts replaced included the Field Programmable Gata Array (FPGA) in the proximity electronics, the $LiNbO_3$ etalon, one of the CCD cameras, the collimator doublet, the liquid crystal variable retarders (LCVRs), the power supply for the LCVR heaters (the heaters on the SUNRISE I flight did not have enough power to bring the instrument to its nominal operational temperature) and the phase-diversity (PD) plate (the original broke upon landing after the SUNRISE I flight). Most of these parts were replaced by nearly identical ones. In addition, the windows of both CCD cameras were removed in order to avoid fringes that had been observed during the SUNRISE I flight.

3. Description of the Mission

SUNRISE II was flown on a zero-pressure stratospheric long-duration balloon, launched and operated by the CSBF. It was launched on 2013 June 12 at 05:37:53 UT (07:37:53 local time) from ESRANGE (67.89°N, 21.10°E) near Kiruna in northern Sweden on a cloudy, but perfectly windstill day. It reached a float altitude of 37.1 km after an ascent lasting approximately

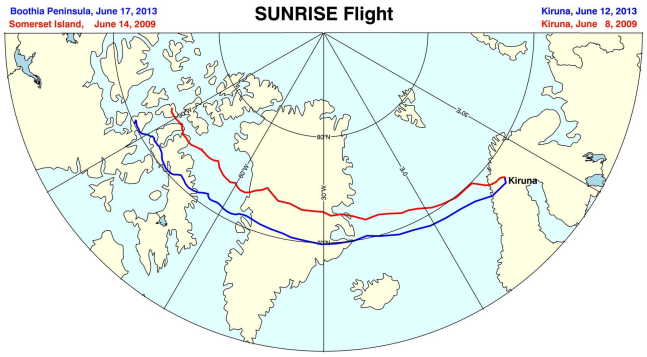

(a)

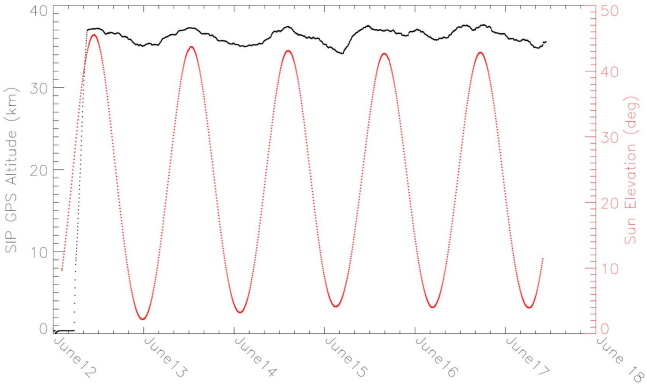

(b)

Figure 3. (a) The flight paths of the 2009 (red curve) and 2013 (blue curve) SUNRISE science flights overplotted on a map of the northern Atlantic. The semi circles mark latitudes of 60°, 70°, and 80°, respectively. (b) The SUNRISE II float altitude vs. time as recorded by the CSBF-provided Support Instrumentation Package (SIP), from shortly before launch up to the time of cut-off from the balloon (black curve, referring to the left axis). Also plotted is the solar elevation angle, as seen from SUNRISE II (in red, referring to the axis on the right).

3.5 h. It then drifted westward at a mean speed of 35.3 km hr^{-1} and at a mean altitude of roughly 36 km. Compared to SUNRISE I it travelled more to the south and somewhat faster across the Atlantic and Greenland, so that it reached the peninsula of Boothia in northern Canada on 2013 June 17 where the flight was terminated at 11:49:24 UT. After 122.3 hr at float altitude the balloon was cut off and the payload descended suspended from a parachute, reaching the ground at 70.08°N, 94.42°W about one hour later. It landed relatively softly but tipped over forward, so that the front ring of the telescope and the radiators of the heat rejection wedge thermal control system were damaged. Otherwise very little serious damage was incurred. Figure 3(a) shows the flight path of SUNRISE II overplotted on a map. Also plotted, for comparison purposes, is the flight path taken by SUNRISE I almost exactly four years earlier. Figure 3(b) displays the height profile of the flight, with the day–night cycles being visible (although the Sun never quite set on the payload at float altitude). Rapid, although usually not very large, increases in height, for instance on June 15 starting at 05:04 UT, are due to ballast drops. The elevation of the Sun as visible from SUNRISE II is overplotted. Clearly, the payload remained in direct sunlight during the entire flight, although the Sun was just over the horizon around local midnight.

Since at float altitude the payload was above 99% of the Earth's atmosphere, virtually seeing-free observations were possible all the time. Also, the balloon stayed above most of the ozone in the Earth's atmosphere, allowing high-resolution imaging in the UV at 2140, 2795, and 3000 Å, although the residual atmosphere did require excessively long observing times at 2795 Å and, to a smaller extent, at 2140 Å.

E-Link worked until 2013 June 13 at 1:05 UT, i.e., until well after commissioning was completed. Two events occurred after commissioning that impacted the science operations. (1) The temperature controller of the IMaX etalon failed on 2013 June 12 at 23:55 UT, although possibly problems in the communications between IMaX subsystems was the real reason for the failure.

(2) On 2013 June 13 at 7:30 UT, about 23 hr after the observations had started, the highly reflective front face of the heat rejection wedge—a glued, 0.1 mm thin second surface mirror—failed. Due to increased absorption the heat rejection wedge temperature rapidly increased each time the telescope was pointed at the Sun, eventually exceeding the temperature sensor measurement range (whose upper limit lay at 130°C) within a number of minutes (the exact number depended somewhat on the time of day). Therefore, all observing sequences had to be shorter than this interval after this incident, with roughly half an hour in between observing sequences to allow the heat rejection wedge to cool down again. However, the optical quality of the data obtained after the failure of the heat rejection wedge remained the same as before, as a careful inspection revealed.

Table 2
SuFI Observing Modes

SuFI mode	Fraction of observing time
5λ: 2140, 2795, 3000, 3968w, 3968n Å	54%
4λ: 2140, 3000, 3968w, 3968n Å	2%
3λ: 3000, 3968w, 3968n Å	33%
2λ: 3000, 3968w Å	8%
1λ: 3968w Å	3%

Note. 3968w refers to the SuFI channel observed through the 1.8 Å wide filter centered on the line core of Ca II H, while 3968n refers to the channel observed through the 1.1 Å narrow Ca filter.

4. Overview of the Data Recorded during the 2013 Flight of SUNRISE

The total length of time over which observations were made was 122 hours, during which period SuFI recorded 300 GB (60,806 images), while IMaX acquired 68 GB of data (48,129 images). During 16% of the total time at float altitude the CWS loop was closed. The longest time series of SuFI data covers 60 minutes, while the longest currently reduced IMaX time series lasts approximately 17 minutes.

SuFI observed in a variety of modes, differing mainly in the wavelengths sampled. The various modes were recorded at different times of day. Thus the two shorter wavelengths, at 2140 and at 2795 Å, were only recorded close to local noon, when the Sun was the highest in the sky and the absorption due to the atmosphere was minimal. A brief summary of the recorded SuFI data is given in Tables 2 and 3. The plate scale per pixel of SuFI depended on the wavelength and was in the range 0.″01983–0.″02069.

Table 3
List of the Longest SuFI Time Series of Active Region Observations

Start time [UT]	Duration (s)	Filter (Å)	Exp. times (ms)	Cadence (s)	μ	AR	IMaX mode
12.06. 23:39	3528	3000, 3968w, 3968n	500, 100, 500	7.2	0.93	11768	V8-4
13.06. 01:10	741	3000, 3968w, 3968n	500, 100, 500	7.2	0.93	11768	n.a.
17.06. 01:43	528	2140, 3000, 3968w, 3968n	2500, 50, 100, 500	10.8	0.45	11775	V8-4
16.06. 04:37	470	3000, 3968w, 3968n	200, 100, 500	5.1	0.30	11775	V8-4
12.06. 19:59	462	3000, 3968w, 3968n	50, 100, 500	6.0	0.94	11768	L12-6
16.06. 00:43	353	2140, 3000, 3968w, 3968n	2000, 50, 100, 500	10.4	0.71	11770	V8-4
17.06. 06:02	344	3000, 3968w, 3968n	50, 100, 500	5.1	0.43	11775	n.a.
16.06. 05:04	335	3000, 3968w, 3968n	200, 100, 500	5.1	0.30	11775	n.a.
16.06. 00:10	294	3000, 3968w	50, 100	2.5	0.71	11770	n.a.
16.06. 05:54	263	3000, 3968w, 3968n	200, 100, 500	5.1	0.29	11775	n.a.
14.06. 02:58	259	1 × 3000, 5 × 3968w	500, 100	7.6/1.2	0.37	11770	n.a.
17.06. 02:37	214	3000, 3968w, 3968n	50, 100, 500	5.1	0.42	11775	V8-4

IMaX data were dominantly obtained in the V8-4 mode, meaning that the full Stokes vector of the Fe I 5250.2 Å line was recorded at eight wavelength positions, with four accumulations at each wavelength. The wavelengths sampled were centered on −120, −80, −40, 0, +40, +80, +120, and +227 mÅ from line center. The last of these samples a continuum position between the $g = 3$ line and its neighboring Fe I line at 5250.6 Å. Each exposure lasted 250 ms, so that the cadence achieved with the IMaX V8-4 mode was 36.5 s. The plate scale per pixel of IMaX remained unchanged at 0.″05446.

A relatively small amount of IMaX data were also recorded in the L12-6 mode, in which only Stokes I and V are recorded at 12 wavelength points in the line, with six accumluations per wavelength point.

5. Data Reduction

Due to the changes in the instrumentation as well as the experience gained from SUNRISE I, the data were reduced using a modified reduction pipeline.

5.1. SuFI

The SuFI data, as on the first flight, were acquired in PD mode, i.e., one half of the sensor was located in the focal plane, while the other half imaged the same part of the solar surface as the first half, but with a fixed offset in the focus direction. This configuration is necessary, since aberrations of the telescope, although small enough to allow for diffraction limited performance at visible wavelengths, are not negligible at the much shorter UV wavelengths. The PD technique in principle allows for the determination and subsequent removal of these aberrations, provided one of the pair of images is in or very near focus according to Gonsalves & Chidlaw (1979) and Paxman et al. (1992).

Therefore, after the traditional darkfield and flatfield corrections, the data were restored using the Multi-Frame Blind Deconvolution (MFBD) wavefront sensing code (van Noort et al. 2005), which allows for an arbitrary PD term to be present in the data. Due to the highly non-telecentric configuration of the beam, however, the image scale of the defocused image was slightly different from the image scale in the focal plane, so that the influence of the tip-tilt components of the wavefront aberrations in the defocused channel differed from those in the focal plane. This effect was accommodated by restoring the frames in the "calibration mode" of the MFBD code, where all fitted wavefront modes are constrained to be the same for the two channels, with the exception of the tip-tilt and focus terms, which are allowed to vary, but with the difference between the focus and defocus channels constrained to have the same value for all PD pairs in the data set. Due to the relatively low frame rate of the SuFI camera, only four PD pairs, recorded in approximately twenty seconds, could be combined to restore each frame, beyond which the solar evolution started to degrade the result.

Although this method worked well on some of the data, it did not always restore the data to the same quality. This is believed to be the result of residual pointing errors during the relatively long exposure time, that blurred the image in a way that is not consistent with the model, which assumes the point-spread function (PSF) to be produced by a single, static wavefront. The azimuthally averaged Fourier power spectrum of the best frames, however, shows power significantly above the noise floor, at wave numbers up to 85% of the true diffraction limit of $D_{\rm telescope}/\rm lambda$ (DL, see for instance Paxman et al. 1996), which is slightly better than the criterion of $D_{\rm telescope}/(1.22\lambda)$ proposed by Rayleigh (1879) and generally adopted for considering individual features to be resolved.

5.2. IMAX

The reduction applied to the data from the 2009 flight was explained in detail by Martínez Pillet et al. (2011a). Consequently, here we focus on changes in the data reduction with respect to the reduction of the first flight's data, necessitated by the replacement of several components of IMaX (described in Section 2.2). These replacements influenced various instrumental effects of IMaX such as the occurrence of fringes, ghost images, and the instrument's stray-light behavior.

After the data were corrected for dark current and flat-field effects, residual excess power due to interference fringes was filtered out in the Fourier domain. Before and after each observing run during the flight, a PD measurement was obtained by inserting a glass plate into the optical path of the first camera in order to record pairs of defocusd and focused images, which then allowed retrieval of the system's PSF. The observational data were reconstructed by applying a modified Wiener filter constructed from the PD PSF. By spatially replicating the images before performing operations in the Fourier domain, a reduction of the fields of view (FOVs) as a side effect of a necessary apodization could be avoided. Hence

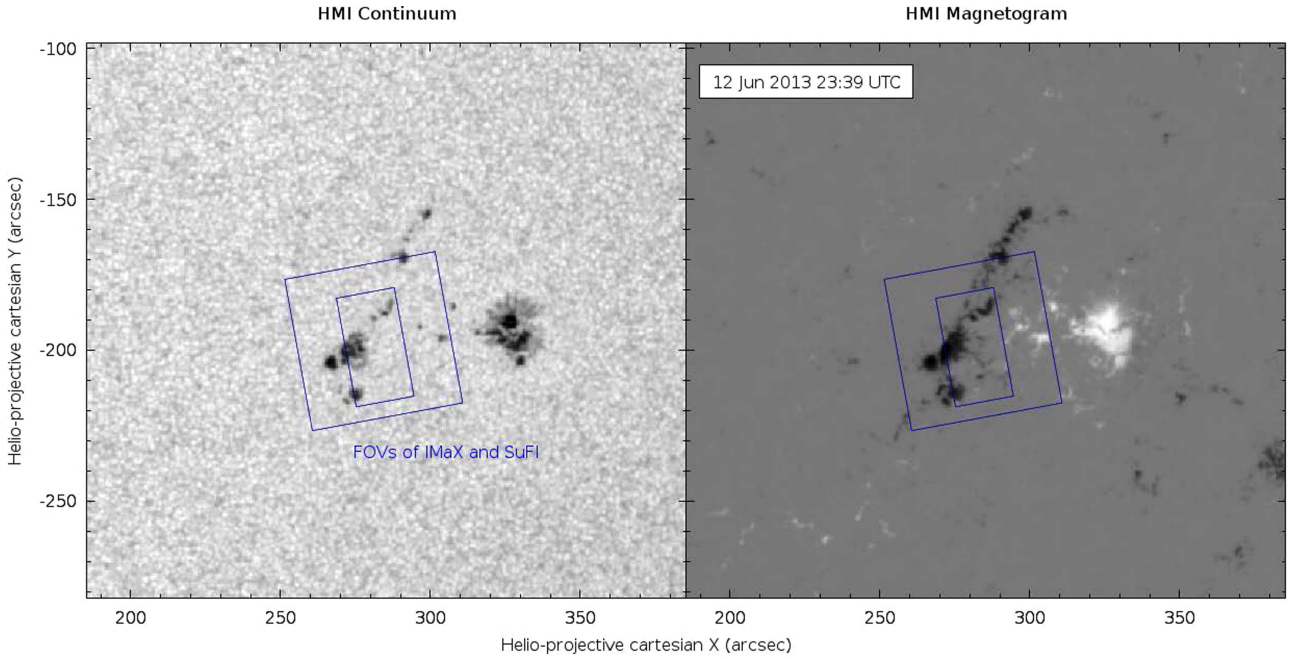

Figure 4. HMI continuum map (left image) and HMI magnetogram (right image) recorded on 2013 June 12 at 23:39 UT, at the beginning of the SUNRISE II time series. The x and y scales are in helio-projective cartesian coordinates and are in arcsec, with the origin located at solar disc center. The outer blue box indicates roughly the FOV of the IMaX instrument, while the inner blue box does the same for the SuFI instrument. The animation of this figure shows the evolution of the active region for three days around the SUNRISE II observations.

(An animation of this figure is available.)

the effective FOV of the IMaX data from SUNRISE II is $51'' \times 51''$.

The instrumental polarization was removed from the observations by a demodulation matrix determined from the pre-flight polarimetric calibration. In contrast to the first flight, this time the FOV dependence of that matrix was taken into account. Since the on-ground polarimeric calibration did not include the main mirror of the telescope and because the thermal environment during calibration was different to the in-flight situation, cross-talk with Stokes *I* had to be removed from the data. Then the images of the two cameras were co-aligned and merged.

In addition, a slight periodic motion of the image was removed, that was not present in the data of the first flight and correlated well with the switching period of the heating power of the LCVRs, which were mounted near one of the folding mirrors. We also added a further step to the data reduction pipeline that interpolated the spectral scans with respect to time in order to compensate for the solar evolution during the IMaX cycle time of 36.5 s.

Finally, we determined the spatial mean Stokes *I* profile and subtracted 25% of the mean profile from the individual profiles to correct the data for 25% global stray light. This is equivalent to deconvolving the IMaX data with a constant stray light not varying over the FOV. Details of the stray-light properties of IMaX can be found in Riethmüller et al. (2017).

The physical quantities of the solar atmosphere were then retrieved from the reconstructed Stokes images via the Stokes-Profiles-INversion-O-Routines (SPINOR; Frutiger 2000; Frutiger et al. 2000), which uses the STOPRO routines to solve the Unno–Rachkovsky equations (Solanki 1987). A relatively simple inversion strategy was applied to get robust results: three optical depth nodes for the temperature (at $\log\tau = -2.5, -0.9, 0$) and a height-independent magnetic field vector, line of sight velocity, and micro-turbulence. The synthetic spectra were not only calculated for the Fe I 5250.2 Å line but also for its neighboring lines (Co I line at 5250.0 Å and the Fe I line at 5250.6 Å) to include their influence. The spectral resolution of IMaX was taken into account by convolving the synthesized spectra with the spectral transmission profile of IMaX measured in the laboratory during a pre-flight calibration campaign (see the bottom panel of Figure 1 in Riethmüller et al. 2014).

The SPINOR inversion code was run for ten iterations, then the output maps of the individual parameters were spatially smoothed and used as the initial guess parameters to a further run of ten iterations. The intermediate smoothing of the free parameters of the inversion was introduced to get rid of spatial discontinuities in the physical quantities that can occur if the inversion gets stuck in local minima of the merit function at individual pixels or groups of pixels. This procedure was repeated five times (implying 50 iterations in all), with a gradually decreasing amount of smoothing. Finally, the resulting LOS velocity maps were corrected for the etalon blueshift, which is caused by the collimated setup (see Martínez Pillet et al. 2011a).

6. Examples of Data and Science Results

6.1. NOAA AR 11768

The longest time series obtained by SUNRISE II was focused on NOAA AR 11768 at $\cos\theta = \mu = 0.93$, where θ is the heliocentric angle. The observations were made on 2013 June 12, starting at 23:39 UT, about 1.5 days after the initial appearance of the active region, at a time when magnetic flux was still emerging. At that time the active region had developed a full-fledged leading polarity sunspot, while the following polarity was mainly concentrated in a string of pores.

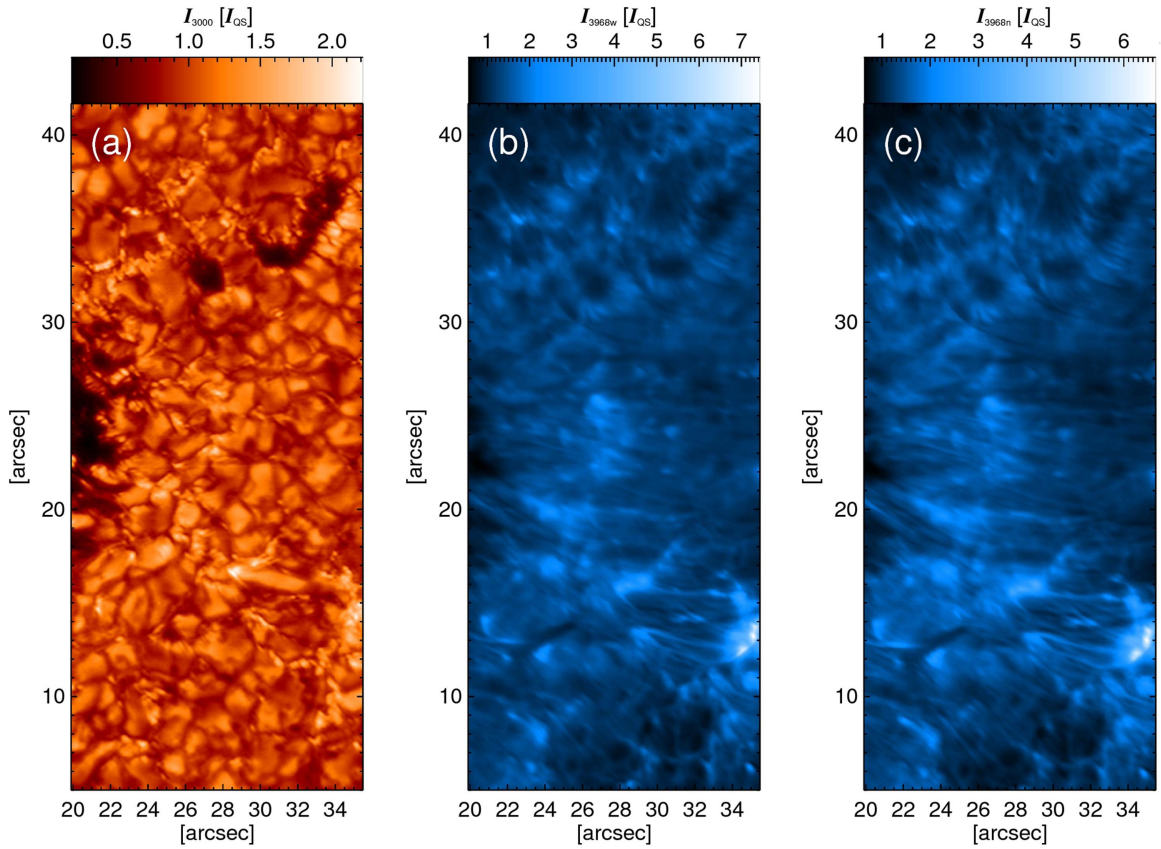

Figure 5. Images recorded by SuFI on 2013 June 12 at 23:46 UT after multi-frame blind deconvolution incorporating phase diversity. Plotted are (a) the intensity in the filter centered on 3000 Å, (b) intensity in the broad Ca II H channel and, (c) in the narrow Ca II H channel. All intensities are given in units of the mean quiet-Sun intensity. The coordinates are given with respect to the lower left corner of the IMaX images (see Figure 7). Note that in this figure the plots at various wavelengths are aligned with each other to an accuracy of only roughly 1″.

The active region is illustrated in Figure 4 at the time of the SUNRISE II observations. The IMaX and SuFI FOVs are overplotted on a Helioseismic and Magnetic Imager (HMI) continuum image and an HMI magnetogram and are indicated by the blue boxes.[12] IMaX covered most of the following magnetic polarity pores, including the largest one. The largest pore had a complex structure and on one side showed a feature with a roughly penumbral brightness exhibiting elongated structures. In the course of the further development, however, this feature did not develop into a proper penumbra (as can be deduced from the animation of Figure 4). The IMaX FOV also contained some of the leading polarity flux, mainly in the form of facular magnetic elements. SUNRISE II also caught a region of emerging flux, to be found in the central southern part of the IMaX FOV and partly in the much smaller SuFI FOV, which captured mainly the region between the two polarities, including one of the emergence events.

The animated Figure 4 shows the evolution of the active region from the very first emergence 1.5 days prior to the start of SUNRISE II observations of this region to approximately 1.5 days after the end of the observations of this region. A significant amount of flux appeared in the day after the SUNRISE II observations, which led to the formation of a proper following polarity sunspot, as well as to an increased size of the leading polarity spot, mainly through the coalescence of pores, many of which already carried a piece of penumbra on one side prior to merging. The blue boxes overlaid on the images in the animated figure are tilted by the rotation angle relative to solar north and the roughly 5° of rotation during the course of the SuFI time series is taken into account. Note that the animated Figure 4 runs at a slower speed during the time of the SUNRISE II observations of this region.

6.2. Sample SuFI Data

The SuFI instrument during the second flight of SUNRISE provided diffraction-limited images at 3000 Å and at 3968 Å in both the broader and the narrower channel centered on the core of the Ca II H line. An image at each of these wavelengths is plotted in Figure 5. Note that during this, the longest time series obtained by SuFI, no data in Mg II k, nor in the 2140 Å channel were obtained due to the low solar elevation at that time and the consequent high atmospheric absorption at these wavelengths.

Strongly different structures are seen at 3000 Å and in the Ca II H line, with the shorter wavelength displaying granulation (as had already been noticed in the SUNRISE I data, e.g., Hirzberger et al. 2010; Solanki et al. 2010), but also bright points (Riethmüller et al. 2010), pores with internal fine structure, and a bright elongated granule located at approximately 30″–32″ in the x-direction and 15″–16″ in the y-direction. This last feature is found to be associated with

[12] The SuFI FOV in Figure 4 is the maximum that can be retrieved from the detector. The width of the images shown in Figure 5 is lower for two reasons: if the broadest possible FOV is used, then the quality of the reconstruction is lower and hence the resolution is less high than in the images displayed in Figure 5. Furthermore only the common FOV of the various SuFI wavelength channels is plotted in Figure 5. Due to differential offsets, this is smaller than the FOV of each individual channel.

magnetic flux emergence. The two brightest features in the 3000 Å image are located near the two ends of this structure; on its left it brightens to the level of a strong bright point, while there is a bright facular region right at the edge of the FOV in the continuation of the elongated granule on its right side.

The surprising lack of difference between the broader and narrower Ca II H channels in Figure 5 suggests that they were observing very similar layers of the Sun. Possibly, the filter selecting the narrower channel had drifted in wavelength (e.g., due to temperature changes in the instrument) and was not centered exactly on Ca II H_3. Due to the similarity between the broad and the narrow Ca II H channels, in the following the discussion will concentrate on the narrower channel.

In the Ca II H images the dominant structures are slender fibrils directed roughly across the SuFI FOV, many of which seem to emanate from the large pore just to the left of the SuFI image. They appear to be similar to those observed earlier by Pietarila et al. (2009). Although most of the filaments seem to roughly follow the same direction, a number of them do cross each other. This is particularly clearly seen close to the location of the emerging magnetic flux mentioned above, at around (30″–34″, 13″–15″). Very likely this is due to fibrils belonging to previously existing magnetic field overlying those associated with the emerging flux that are directed differently. The lengths of these fibrils are hard to determine, due to inhomogeneities that may be present in the background, but some seem to extend over a fair portion of the width of the SuFI images. Strikingly, the fibrils are also constantly evolving and in motion. The lengths, along with other properties of these fibrils, are studied in a further paper in this special issue (Gafeira et al. 2017b), while the dynamics of the fibrils, in particular wave modes travelling along them, are investigated by Jafarzadeh et al. (2017b) and by Gafeira et al. (2017a).

The brightenings seen at 3000 Å in connection with the flux emergence are also visible in Ca II H. The magnetic flux emergence caught by IMaX and SuFI is investigated by Centeno et al. (2017) and Danilovic et al. (2017). At a later stage during the time series this brightening develops further into a small flare that engulfs the emerging flux region and is prominently visible in the Ca II H line.

SuFI on board SUNRISE II also obtained the first high-resolution images in the Mg II k line, which have already been published in two earlier papers (Riethmüller et al. 2013a; Danilovic et al. 2014). Images taken in the Mg II k filter were found to have considerable similarity with nearly simultaneously recorded Ca II H images, although some distinct differences were also found. These included a 1.4–1.7 times larger intensity contrast and a more smeared appearance. Exampls of Mg II k images of the quiet Sun and of a weak plage/enhanced network region are shown in Figure 6. These images were exposed for 50 s to counter the strong atmospheric absorption at this wavelength and to obtain a sufficient signal-to-noise ratio. The images are based on SuFI level 3 data, i.e., data that have been PD reconstructed using wave-front errors averaged over the whole time series of images. See Hirzberger et al. (2011) for more details on reduction and PD reconstruction of SuFI data.

It was concluded that some of these differences may be caused by the much longer integration time needed to record the Mg II k images due to the strong ozone absorption at that wavelength, while others are likely intrinsic. Possible reasons for the intrinsic differences given by Danilovic et al. (2014)

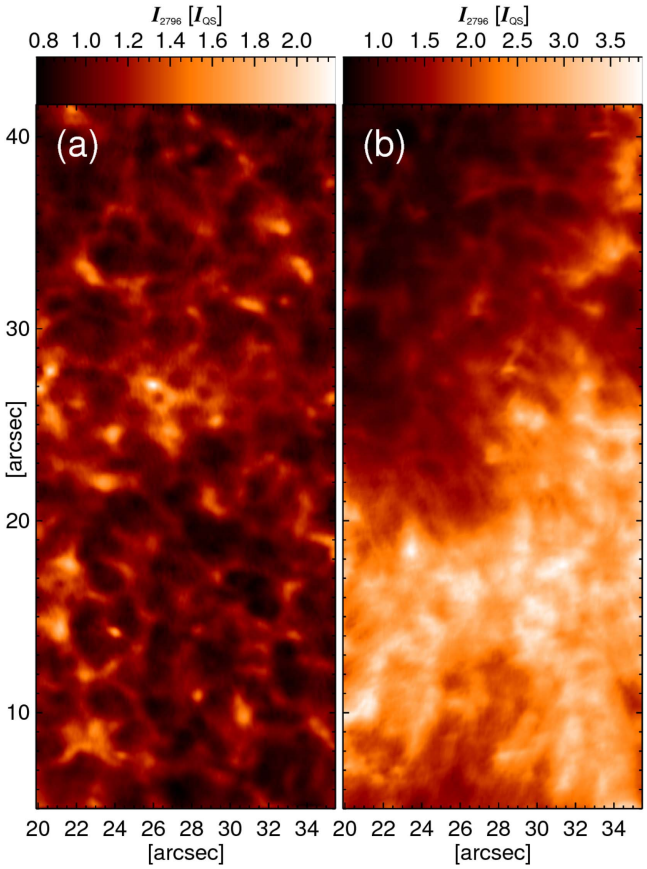

Figure 6. Images recorded by SuFI in the Mg II filter. Panel (a) displays a part of the quiet Sun recorded on 2013 June 13 at 12:52:50 UT, while in panel (b) a weak plage is shown that was observed on 2013 June 12 at 12:50:48 UT. Both images were recorded exactly at disc center and correspond to SuFI level 3 data (see the main text for details) and have been PD reconstructed using an averaged point-spread function.

include greater formation height and greater formation height range of the Mg line (the latter due to the rather broad Mg filter) and the stronger response of the emission peaks of Mg II k to temperature.

6.3. Sample IMaX Data and Inversion Results

The continuum intensity in the visible recorded by IMaX at +227 mÅ from the line center is plotted in Figure 7(a). IMaX images contain a larger number of pores than SuFI due to the bigger FOV. As expected for the continuum intensity at 5250 Å, bright points are much less prominent than at 3000 Å (Figure 5(a)), although the fine structure in the largest pore is clearly visible, with some of the bright "umbral dots" being among the brighter structures in the image. Also clesrly visible in that figure is the long elongated granule already pointed out in the 3000 Å image (located at (30″, 15″) in the IMaX FOV). Another similar granule is found to its right. Both are associated with magnetic flux emergence.

The bright points in the line core image displayed in Figure 7(b), often forming connected chains filling the intergranular lanes, possess a high contrast. Here, what we refer to as the line core intensity is simply the intensity at the central IMaX wavelength point, which is nominally located at the wavelength of the Fe I 5250.2 Å line core. Chains of such bright points surround most of the pores, but the most prominent bright feature in this image is the strong brightening

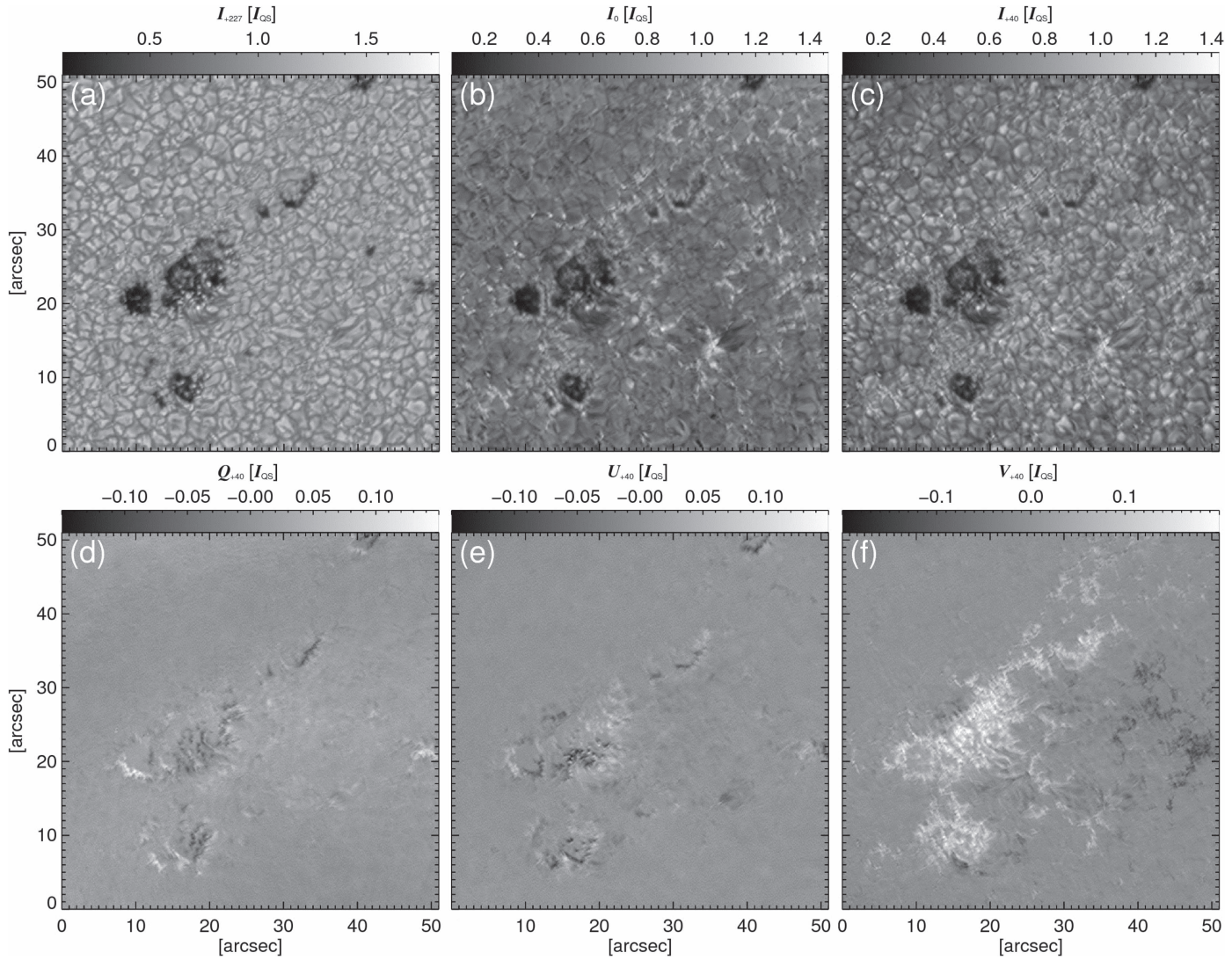

Figure 7. IMaX observables recorded on 2013 June 12 at 23:46 UT after PD reconstruction. Plotted are (a) the continuum intensity, I_{+227}, (b) line core intensity (i.e., intensity in the wavelength channel nominally located at the line core), (c)–(f) the Stokes I, Q, U, and V values at +40 mÅ from the line center. All quantities are given in units of the respective quiet-Sun intensity, I_{QS}.

located between the two elongated granules, i.e., between the two small flux emergence events. The line core of Fe I 5250.2 Å obviously forms below the height of formation of the radiation sampled by either of the two SuFI Ca II H filters, as the iron line core image still shows faint vestiges of granulation and no signs of fibrils. All quantities in Figure 7 are normalized to the respective intensity averaged over two areas within the joint IMaX and SuFI FOV with near-quiet-Sun conditions, i.e., a relatively low magnetic flux density. We call this averaged "quiet-Sun" intensity, I_{QS}. Note that the granule pattern changes to that of reversed granulation if instead of being divided by I_{QS}, as is the case in Figure 7(b), the line core intensity is divided by the local continuum intensity, i.e., I_{+227}, at each pixel (Kahil et al. 2017).

Stokes I, Q, U, and V in the red flank of 5250.2 are plotted in Figures 7(c)–(f). The differences between Figure 7(c) and Figures 7(a) and b are due to the formation height of the line flank (at +40 mÅ) lying between those of the other two wavelengths and the fact that the intensity in the line flank, i.e., in Figure 7(c), is very sensitive to the Doppler shift of the spectral line. The intensity in the line core, as plotted in Figure 7(b), is also affected by Doppler shifts, but to a much lesser extent than the line flanks.

Maps of the best-fit parameters obtained from the inversion of the IMaX Stokes vectors illustrated in Figure 7, are presented in Figure 8. The panels in the upper row display the temperature at the three nodes at which it was determined, $\log(\tau) = 0$, $\log(\tau) = -0.9$ and $\log(\tau) = -2.5$; the lower panels give the magnetic field strength, B, the inclination of the magnetic field relative to the line of sight, γ, and the line-of-sight velocity, v_{LOS}.

The results of the inversions reveal some conspicuous features. Among these are the strong blue- and redshifts in the granulation (note that we have not removed the p-modes from the inverted data, so the velocities are influenced by such oscillations). The velocity amplitude is larger than in the granulation shown by Solanki et al. (2010). An important reason for this is that scattered light has been removed from the present data, while the data analyzed by Solanki et al. (2010) were still affected by scattered light. Some discrepancy can also be introduced because the velocities displayed by Solanki et al. (2010) were obtained from a Gaussian fit to line profiles

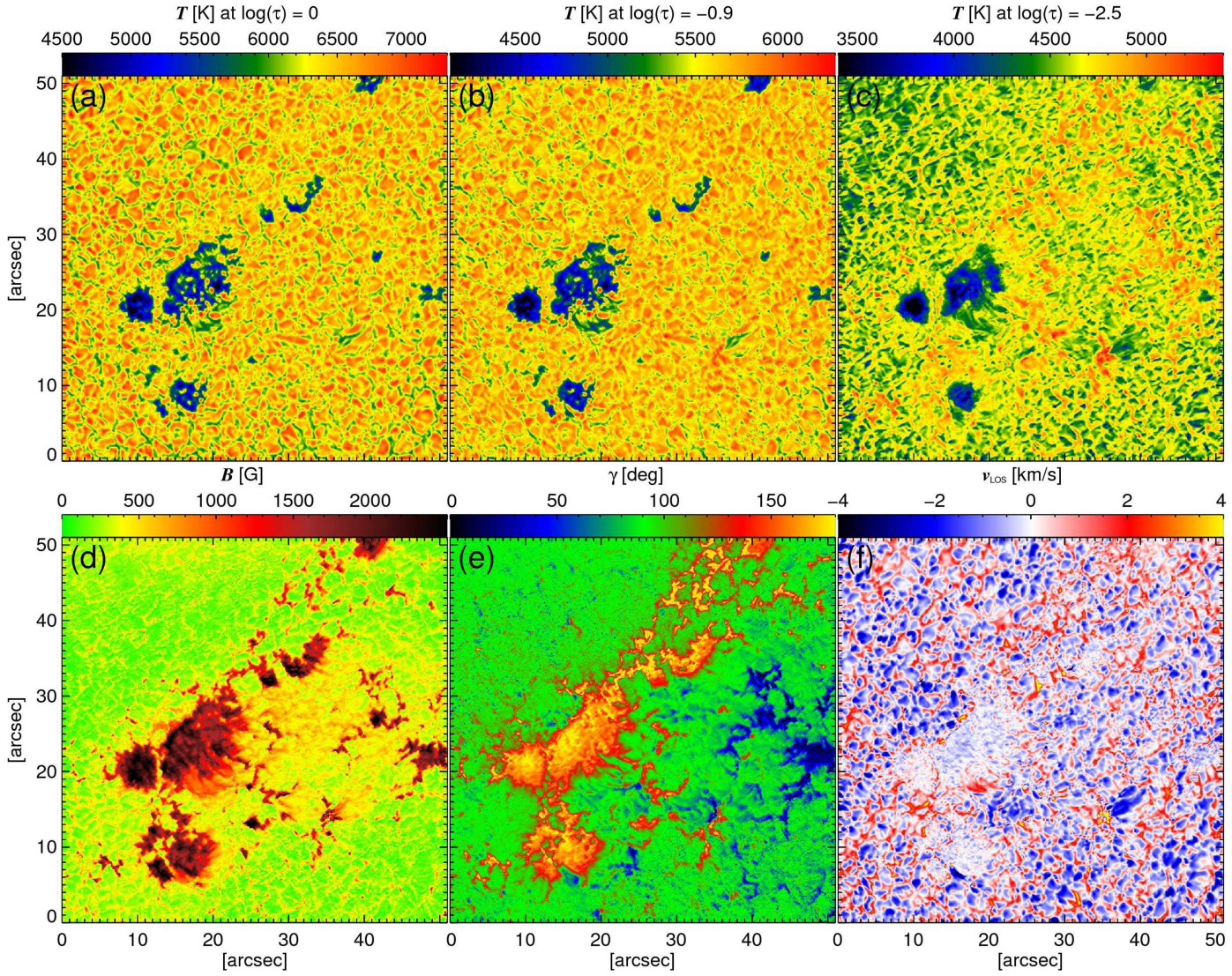

Figure 8. Best-fit atmospheric parameters deduced from the inversion of the Stokes vectors recorded by SUNRISE/IMaX and shown in Figure 7. Upper row of panels, (a)–(c): temperature T ($\log\tau = 0$), T ($\log\tau = -0.9$) and T ($\log\tau = -2.5$). Lower row, (d)–(f): magnetic field strength, B, magnetic field inclination, γ, and the line-of-sight velocity, $v_{\rm LOS}$. Postive velocities indicate downflows. γ is relative to the line of sight direction.

sampled at four wavelengths, while the velocities presented here were provided by the SPINOR inversions of line profiles sampled at seven wavelength points. One of the emerging flux patches is found to be associated with a strong blueshift, much stronger than the other emerging flux feature.

6.4. Pores

One noticeable feature of the inversion results is that the photospheric field strength in pores often reaches 2500 G (comparable with the highest values found from *Hinode* data after deconvolving with the PSF; Quintero Noda et al. 2016). In some places higher field strengths are reached, but these cannot be trusted due to the limited wavelength range of the observations and the fact that the continuum point at +227 mÅ starts to be affected.

Another striking feature is that, whereas all pores are clearly cooler than their surroundings at the two lower heights ($\log\tau = 0$, -0.9), only the larger pores are clearly distinguishable from their surroundings in the temperature map at $\log\tau = -2.5$. The smaller pores can hardly be separated from their surroundings. In contrast, the line core image in Figure 7 shows a darkening also at the locations of the smallest pores. However, this is mainly due to the lower continuum intensity at these locations. Also, the line core is affected by the Zeeman effect and to a smaller extent also Doppler shifts, so that it is not an unalloyed measure of the temperature. In order to test whether the inversions are giving a reasonable representation of the temperature stratification in pores we consider the SuFI Ca II H channel.

To compare SuFI and IMaX data the images at individual SuFI wavelengths were aligned to sub-pixel accuracy with the most similar IMaX images. For 3000 Å this is the 5250.4 Å continuum, while the Ca II H channel is compared with the IMaX line core, normalized to I_{+227} at each pixel individually (then the images look more similar). More information on the procedure are provided by Kaithakkal et al. (2017); see also Jafarzadeh et al. (2017b).

Thumbnails of T at $\log\tau = 0$, -0.9 and -2.5 as well as of IMaX continuum intensity, I_{+227}, and the intensity in SuFI 3000 and 3968n Å channels ("n" is for the narrow Ca II H channel introduced in Section 2.2) are plotted in Figure 9 for

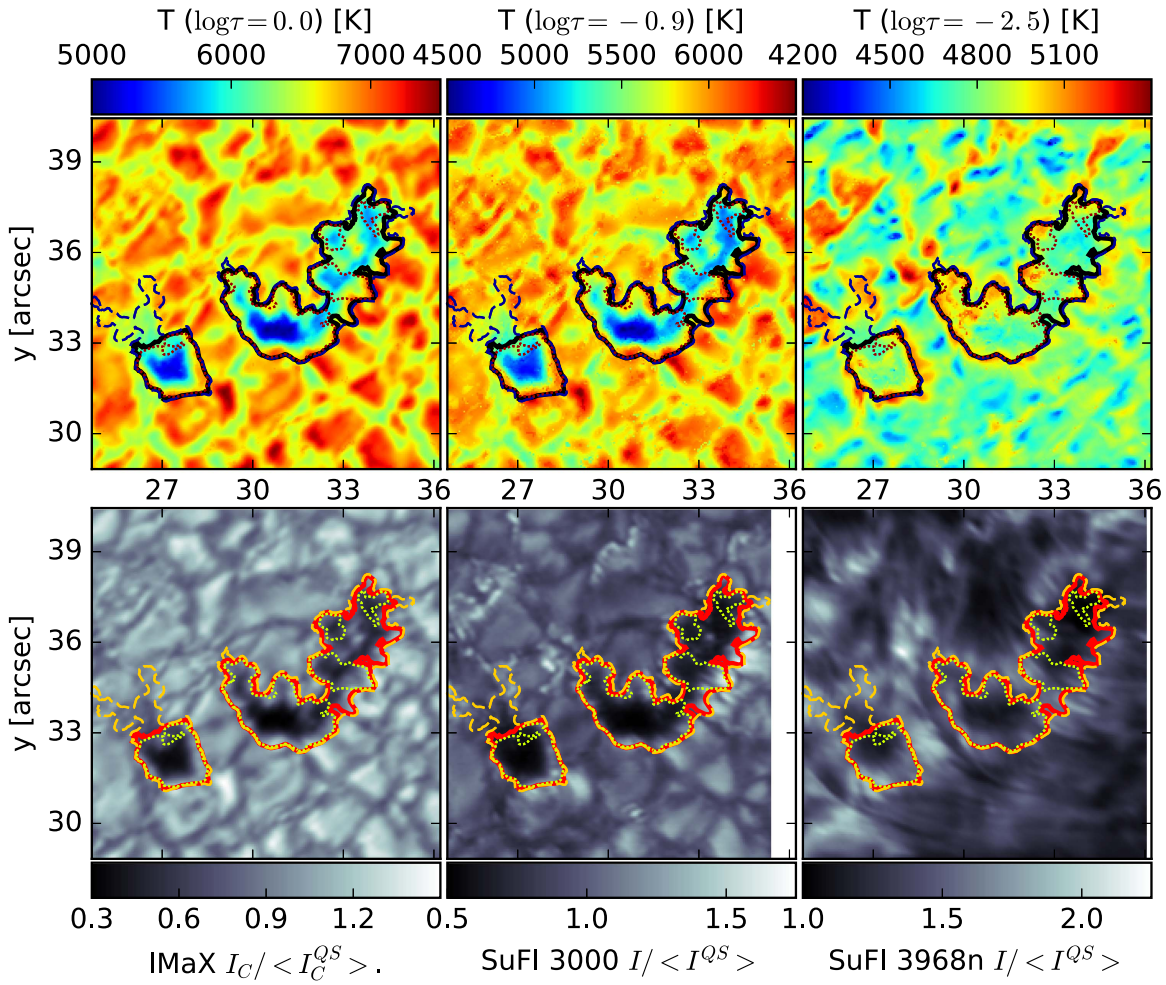

Figure 9. Blow-ups of a region containing two pores within the SuFI FOV. Upper row of panels, from left to right: temperature T ($\log\tau = 0$), T ($\log\tau = -0.9$) and T ($\log\tau = -2.5$). Lower row, from left to right: IMaX continuum intensity, I_{+227}, SuFI 3000 Å and SuFI 3968n channel. The solid contours around the pores mark a field strength of 1400 G. For illustration purposes, we have added contours corresponding to 1200 G (dashed) and 1600 G (dotted). In the lower panels the contours have been given different colors to enhance clarity.

two small pores in the top-right part of the SuFI FOV, and in Figure 10 for a single, very small, somewhat weaker pore in the lower part of the SuFI FOV. Overlaid on both pores are contours of the 1400 G level of the magnetic field. In the following, we consider this contour as an independent boundary of the pore, or more exactly of the magnetic concentration underlying the pore.

1400 G is found to be a good compromise, on the one hand, to isolate a pore from the bright points in its neighborhood while, on the other hand, keeping as much of the pore as possible within the contour. For example, if we take 1200 G or 1300 G, then the bright points often found in the immediate vicinity of pores are included in the contours of some of the pores. If, however, we use a larger value, such as 1500 G or 1600 G, then we include less of the dark part of the pore in the contour. To illustrate this we have added also contours of 1200 G and 1600 G besides those of 1400 G in Figure 9. The 1200 G contour includes bright extensions from the smaller (lower left) pore in this image, while the 1600 G contour misses a significant fraction of the upper right pore.

Interestingly, the 1400 G contour often lies outside the actual pores as seen in, e.g., I_{+227} or the SuFI 3000 Å channel. When comparing with I_{+227}, a part of this difference may have to do with the expansion of the field with height. However, the difference in size is just as large when considering the temperature at $\log\tau = -0.9$, which is much closer to the height at which the magnetic field is determined. Hence, these images demonstrate that pores are surrounded by regions of strong magnetic field that extend well beyond the visible boundaries of the individual pores (see also Martinez Pillet 1997). Of course, the magnetic field, being determined from multiple recordings, is more susceptible to jitter, and may not have the same high resolution as the individual images it is compared with. This extension of strong fields beyond the boundary of the pore still holds even if we consider a threshold of 1500 G or even 1600 G, even though some of the dark parts of the pores no longer lie within the 1600 G contour.

Figures 9 and 10 confirm that the temperature in the lower two inversion nodes are clearly lower than in the surroundings, but are rather similar in the upper node. Similarly, in I_{+227} and at 3000 Å the pores are all clearly dark, while in Ca II H the picture is more mixed. Whereas the pore in Figure 10 is clearly as bright as its surroundings and even has a particularly bright intrusion, the pores seen in Figure 9 both appear to be somewhat darker than their immediate surroundings.

We note, however, that the immediate surroundings of the pores in the Ca images are relatively bright (see Figure 5). The pores are often surrounded by considerable magnetic flux that

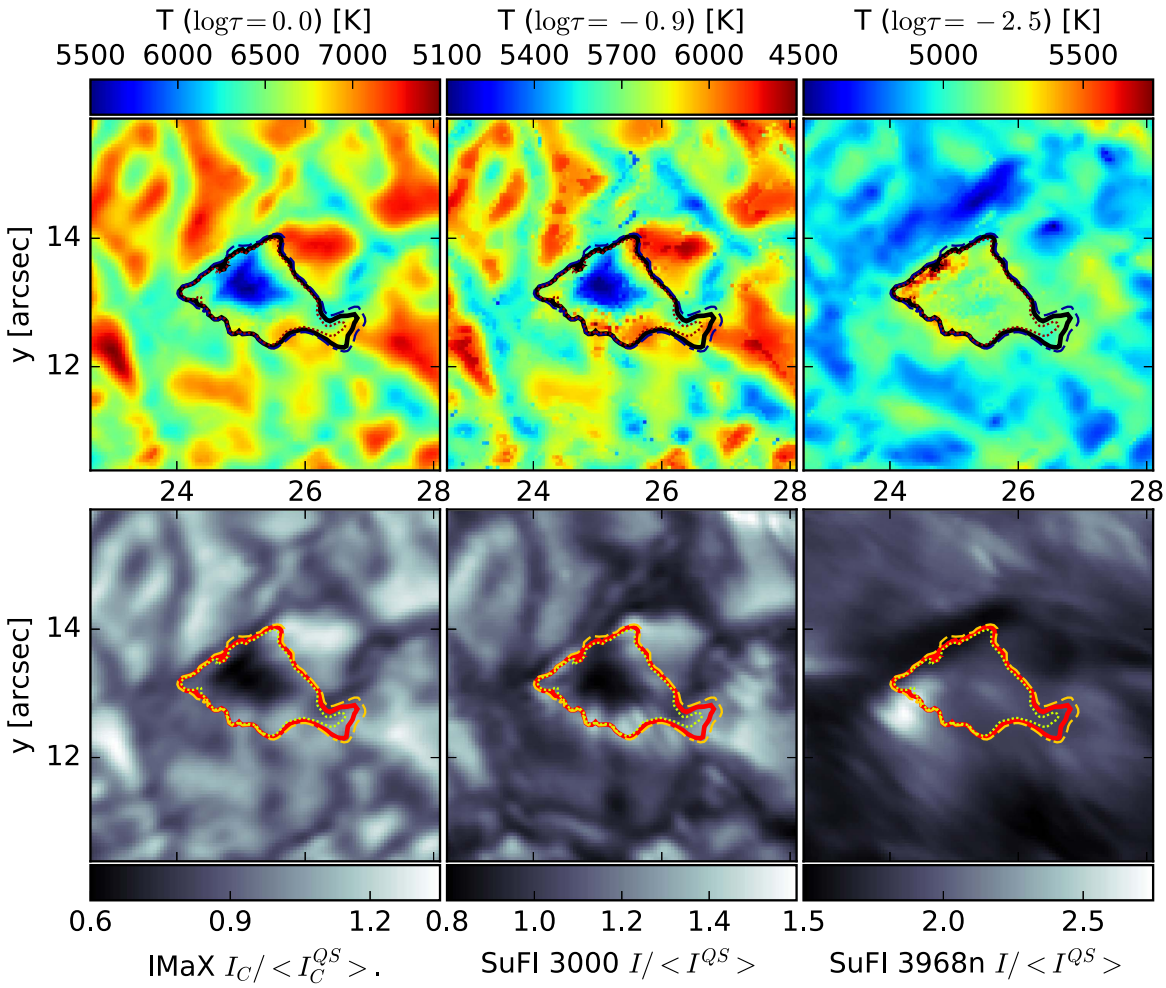

Figure 10. The same as Figure 9, but for a single small pore.

produces a local brightening. In radiation coming from the lower photosphere, some of this is visible as bright points, or particularly bright granules or granule walls (similar to faculae near the limb, e.g., Carlsson et al. 2004; Keller et al. 2004; Lites et al. 2004). In the low chromosphere, however, this concentration of magnetic flux produces enhanced brightenings in the form of mainly short fibrils surrounding the pores. The pores are not substantially darker than other, less bright parts of the solar surface in the Ca II H filter (see Figure 5).

To study this more quantitatively, we plot the corresponding histograms in Figures 11 and 12. Each set of histograms represents either the three temperatures, at $\log\tau = 0, -0.9, -2.5$ (left panels), or the three intensities (IMaX I_{+227}, SuFI 3000 Å, SuFI 3968n Å; right panels) studied here. All intensities and temperatures in Figures 11 and 12 are normalized to patches of comparatively quiet Sun (i.e., with low amounts of magnetic flux) near the top left and the bottom of the SuFI FOV.

In all pores the temperatures in the two lower layers and the intensities at the wavelengths formed deeper (IMaX I_{+227} and SuFI 3000 Å) are predominantly lower than in the quiet Sun. The pixels in which they are higher are often the hot walls of neighboring granules that are seen through a strong magnetic field. The same is true for the intensities in the two deeper-forming wavelengths. The temperature at the top node and the brightness in the Ca II H channel behave quite differently, however. The temperature lies below the quiet-Sun value for only a small fraction of the points. The same is also true for the Ca intensity, for which the ratio of hotter and brighter points to cooler and darker ones is even more extreme.

Hence, although the small pores partly remain visible as dark features relative to their immediate surroundings in the lower chromosphere, they are approximately as bright as, or even brighter than, the quiet Sun at those layers. The most extreme enhancement is displayed by the smallest of the three pores, with the largest being the coolest and darkest (by a small amount) of these three.

The largest pore in the IMaX FOV (and partly in the SuFI FOV) does remain considerably darker than the quiet Sun, even in the Ca images, which unfortunately cover only a small part of the whole pore. Nonetheless, the behavior of the various pores taken together suggests that the difference in the vertical temperature gradient within these pores to that in the quiet Sun depends significantly on the size of the pore. The photospheric temperature gradient is flattest for the smallest pores, with the temperature starting nearly 1000 K below the average quiet-Sun value at the solar surface and reaching the quiet-Sun value in the upper photosphere. For large pores, however, the temperature gradient appears to be more similar to that in the quiet Sun.

Inhomogeneities in brightness and temperature within the pores also decrease with height. Thus, in Figure 9 the umbral

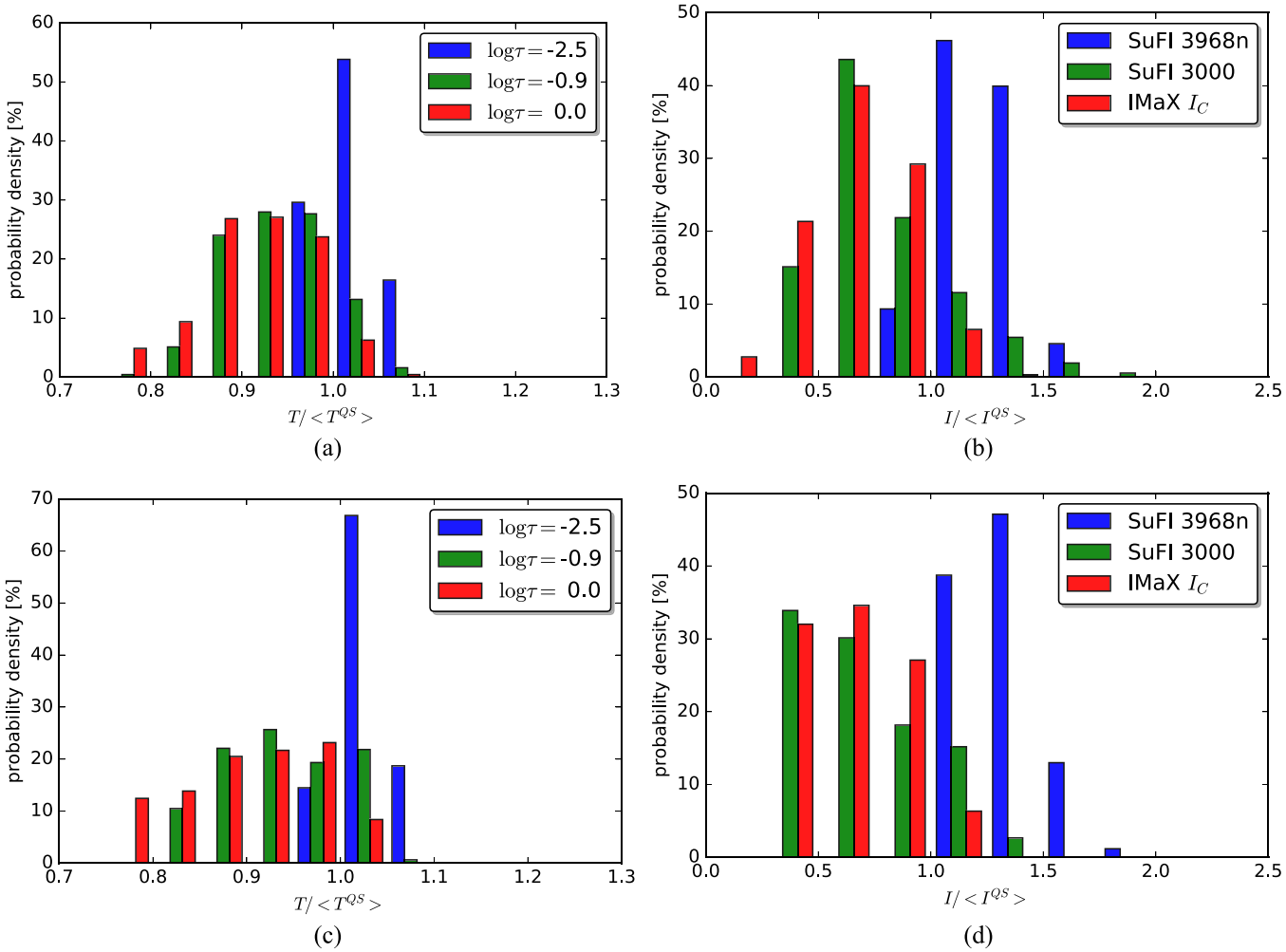

Figure 11. (a) and (c) Histograms of T ($\log\tau = 0$), T ($\log\tau = -0.9$) and T ($\log\tau = -2.5$ within the 1400 G contours of the two pores displayed in Figure 9. (b) and (d) Corresponding histograms of IMaX I_{+227}, SuFI 3000 Å, SuFI 3968n Å. Panels (a) and (b) represent the larger pore, in the upper right part of the images in Figure 9, panels (c) and (d) the pore in the lower left. Histogram colors distinguish between the different $\log\tau$ layers, or wavelengths, as labelled in the individual panels.

dot-like brightenings in the pore at the upper right of the frame are clearly visible in the I_{+227} at 5250.4 Å, but only very weakly visible at 3000 Å, which is formed only about 50 km higher, and cannot be seen at all at 3968 Å. This suggests that such inhomogeneities are likely of convective origin, as proposed by Parker (1979), Choudhuri (1986), and Schüssler & Vögler (2006) for umbral dots. In sunspot umbrae a similar restriction to low heights of the thermal enhancements/ brightenings associated with umbral dots has been found by, e.g., Socas-Navarro et al. (2004) and Riethmüller et al. (2008, 2013b).

7. Conclusions and Outlook

The second science flight of SUNRISE in 2013 June allowed this balloon-borne solar observatory to obtain the first seeing-free observations of an active region close to the diffraction limit of the 1 m diameter telescope. These data are rich in information about a variety of solar phenomena at very high spatial resolution and at wavelengths that partly cannot be accessed from the ground. Below we list some of the findings that have been obtained from these data, most of which are presented in various papers of this special issue.

In the present paper we have, besides providing an overview of the instrumentation and the mission, considered thermal properties of pores as an illustration of the capabilities of the SUNRISE II data. Earlier, the first ever high-resolution images of the quiet and active Sun in the Mg II k line, obtained during the SUNRISE II flight, were reported by Riethmüller et al. (2013a) and Danilovic et al. (2014).

In the special issue a study by Centeno et al. (2017) reports on two emerging flux events, describing in greater detail than previously possible the interrelated dynamics of the gas and the field, as well as the likely occurrence of magnetic reconnection during the emergence. The properties of a likely siphon flow and of the small, initially low-lying loop connecting magnetic elements with a pore are deduced by Requerey et al. (2016b) and the 3D structure of the magnetic field lines and hence of the flow vector are determined. The properties and dynamics of moving magnetic features (MMFs) on one side of the largest pore in the IMaX FOV are deduced by Kaithakkal et al. (2017) and contrasted with the properties of MMFs around sunspots. The proper motion of magnetic bright points in different parts of the quiet Sun and of an active region are analyzed by Jafarzadeh et al. (2017a). They find very different behaviors depending on the location, with the features moving strongly

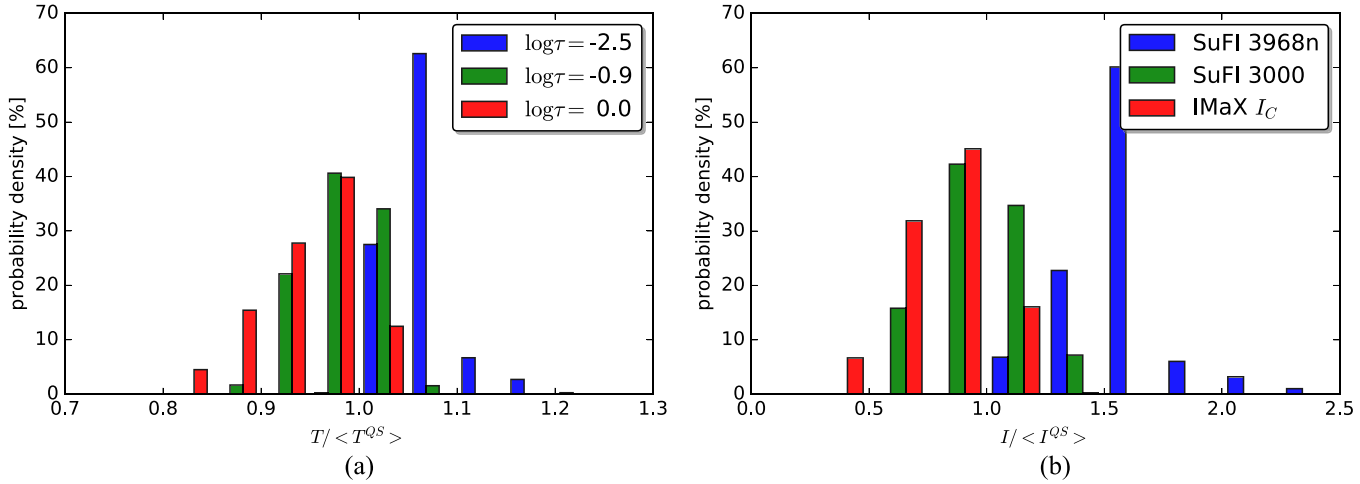

Figure 12. The same as Figure 11, but for the small pore displayed in Figure 10.

superdiffusively in the internetwork, diffusively in the network and in between these extremes in the active region. Riethmüller et al. (2017) present a novel inversion technique employing magnetohydrodynamic (MHD) simulations to provide the model atmospheres needed to compute synthetic Stokes vectors that reproduce the observed Stokes parameters. They illustrate the quality of the inversions by applying the technique to the SUNRISE II polarimetric data.

The properties of the slender fibrils dominating the SuFI Ca II H images are determined by Gafeira et al. (2017a), who show that the fibrils live much longer than a simple analysis would suggest, if one takes into account that they often fade away and reappear after some time. The discovery of ubiquitous transverse waves travelling along these fibrils and carrying copious amounts of energy is reported by Jafarzadeh et al. (2016c), while Gafeira et al. (2017a) present the discovery of compressible waves travelling along the fibrils, which they identify as sausage waves. Jafarzadeh et al. (2017d) find evidence that these slender fibrils seen in Ca II H outline a canopy of magnetic field lying below that known from Hα and Ca II 8542 Å fibril observations.

Chitta et al. (2017) observed that coronal loops are rooted in regions with mixed-polarity fields. They provide evidence for flux cancellation and presence of inverse Y-shaped jets (signatures of magnetic reconnection) at the base of coronal loops that might supply (hot) plasma to the overlying coronal loop. They suggest a revision of the traditional picture in which each loop footpoint is smoothly connected to unipolar regions on the solar surface. Danilovic et al. (2017) compare an Ellerman bomb observed by SUNRISE II with a similar, simulated event in which magnetic reconnection occurs at the location of emerging flux. The 3D radiation–MHD simulation reveals the complexity of the underlying physical process and the limitations of the observational data. Thus, the SUNRISE/IMaX data cannot determine the height at which magnetic reconnection takes place. The authors also show, however, that the velocity and magnetic vector measured at the high resolution of SUNRISE/IMaX reveals how shortcomings of the MHD simulations can be overcome.

Wiegelmann et al. (2017) have computed general linear magneto-static equilibria of the magnetic field and gas using the SUNRISE II/IMaX observations as a boundary condition. In this way they obtain the magnetic field structure in the upper atmosphere without having to assume the validity of the force-free assumption in the solar photosphere. They computed linear magneto-static equilibria for all the IMaX frames of the active region, without the problems faced when modeling the magnetic field in different atmospheric layers of the quiet Sun.

In addition to the exciting results obtained from the SUNRISE II flight briefly mentioned above, the present special issue also contains a number of papers that are based on data from the SUNRISE I flight. These data are still unique in terms of consistently high-resolution polarimetric and UV time series of the quiet Sun. Such papers include the investigation by Requerey et al. (2017a) in which the authors uncover the tight connection between concentrated magnetic fields and convectively driven sinks in the quiet Sun. Kahil et al. (2017) probe the relationship between brightness contrast at UV and visible wavelengths and the magnetic flux in the quiet Sun, finding that the contrast keeps increasing with magnetic flux, unlike most earlier observational results, but in qualitative agreement with MHD simulations. Jafarzadeh et al. (2017c) characterize the wave modes observed at two heights in magnetic bright points, including both compressible waves seen in brightness fluctuations and transverse waves obtained from proper motions. The short travel times suggest large wave speeds. A new estimate of the flux emergence rate in the quiet Sun is obtained by Smitha et al. (2017). Compared with the emergence rate deduced from *Hinode*/SOT data using the same technique, the emergence rate obtained from SUNRISE I data is around an order of magnitude larger.

Clearly, the data from both flights of SUNRISE remain rich in their information content and it is expected that many more results will be gleaned from them in the coming years. In parallel with the scientific analysis of the data, preparations are starting for a third flight of SUNRISE. It is planned that on such a flight the observatory will carry upgraded science instruments as well as new spectropolarimetric ones that provide more information on the magnetic field and its influence on the solar atmosphere, with particular emphasis on the solar chromosphere.

We would like to thank all current and previous team members not listed as co-authors for their valuable contribution to the project. We thank S. Jafarzadeh for useful discussions and helpful comments on the manuscript. We also thank the CSBF team for providing a perfect launch and a good recovery of the payload. The German contribution to SUNRISE and its

reflight was funded by the Max Planck Foundation, the Strategic Innovations Fund of the President of the Max Planck Society (MPG), DLR, and private donations by supporting members of the Max Planck Society, which is gratefully acknowledged. The Spanish contribution was funded by the Ministerio de Economía y Competitividad under Projects ESP2013-47349-C6 and ESP2014-56169-C6, partially using European FEDER funds. The National Center for Atmospheric Research is sponsored by the National Science Foundation. The HAO contribution was partly funded through NASA grant number NNX13AE95G. This work was partly supported by the BK21 plus program through the National Research Foundation (NRF) funded by the Ministry of Education of Korea. L.G. acknowledges research funding from the State of Lower Saxony, Germany. *SDO* is a mission of NASA's Living With a Star (LWS) program. The *SDO*/HMI data were provided by the Joint Science Operation Center (JSOC). The National Solar Observatory (NSO) is operated by the Association of Universities for Research in Astronomy (AURA) Inc. under a cooperative agreement with the National Science Foundation.

Software: Multi-Frame Blind Deconvolution (MFBD, van Noort et al. 2005), Stokes-Profiles-INversion-O-Routines (SPINOR, Frutiger 2000; Frutiger et al. 2000), STOPRO (Solanki 1987).

References

Barthol, P., Gandorfer, A., Solanki, S. K., et al. 2011, SoPh, 268, 1
Beckers, J. M., & Schröter, E. H. 1968, SoPh, 4, 303
Bello González, N., Franz, M., Martínez Pillet, V., et al. 2010, ApJL, 723, L134
Berkefeld, T., Schmidt, W., Soltau, D., et al. 2011, SoPh, 268, 103
Bonet, J. A., Márquez, I., Sánchez Almeida, J., et al. 2010, ApJL, 723, L139
Borrero, J. M., Martínez-Pillet, V., Schlichenmaier, R., et al. 2010, ApJL, 723, L144
Carlsson, M., Stein, R. F., Nordlund, Å., & Scharmer, G. B. 2004, ApJL, 610, L137
Centeno, R., Blanco Rodríguez, J., Del Toro Iniesta, J. C., et al. 2017, ApJS, 229, 3
Chitta, L. P., Peter, H., Solanki, S. K., et al. 2017, ApJS, 229, 4
Choudhuri, A. R. 1986, ApJ, 302, 809
Danilovic, S., Beeck, B., Pietarila, A., et al. 2010, ApJL, 723, L149
Danilovic, S., Hirzberger, J., Riethmüller, T. L., et al. 2014, ApJ, 784, 20
Danilovic, S., Solanki, S. K., Barthol, P., et al. 2017, ApJS, 229, 5
De Pontieu, B., McIntosh, S. W., Carlsson, M., et al. 2007, Sci, 318, 1574
Frutiger, C. 2000, PhD Thesis No. 13896, ETH Zürich
Frutiger, C., Solanki, S. K., Fligge, M., & Bruls, J. H. M. J. 2000, A&A, 358, 1109
Gafeira, R., Jafarzadeh, S., Solanki, S. K., et al. 2017a, ApJS, 229, 7
Gafeira, R., Lagg, A., Solanki, S. K., et al. 2017b, ApJS, 229, 6
Gandorfer, A., Grauf, B., Barthol, P., et al. 2011, SoPh, 268, 35
Gonsalves, R. A., & Chidlaw, R. 1979, Proc. SPIE, 207, 32
Hirzberger, J., Feller, A., Riethmüller, T. L., et al. 2010, ApJL, 723, L154
Hirzberger, J., Feller, A., Riethmüller, T. L., Gandorfer, A., & Solanki, S. K. 2011, A&A, 529, A132
Jafarzadeh, S., Rutten, R. J., Solanki, S. K., et al. 2017d, ApJS, 229, 11
Jafarzadeh, S., Solanki, S. K., Cameron, R. H., et al. 2017a, ApJS, 229, 8
Jafarzadeh, S., Solanki, S. K., Gafeira, R., et al. 2017b, ApJS, 229, 9
Jafarzadeh, S., Solanki, S. K., Lagg, A., et al. 2014, A&A, 569, A105
Jafarzadeh, S., Solanki, S. K., Stangalini, M., Cameron, R. H., & Danilovic, S. 2017c, ApJS, 229, 10
Ji, H., Cao, W., & Goode, P. R. 2012, ApJL, 750, L25
Joshi, J., Pietarila, A., Hirzberger, J., et al. 2011a, ApJL, 734, L18
Joshi, J., Pietarila, A., Hirzberger, J., et al. 2011b, ApJL, 740, L55
Kahil, F., Riethmüller, T., & Solanki, S. K. 2017, ApJS, 229, 12
Kaithakkal, A., Riethmüller, T., Solanki, S. K., et al. 2017, ApJS, 229, 13
Katsukawa, Y., Berger, T. E., Ichimoto, K., et al. 2007, Sci, 318, 1594
Keller, C. U., Schüssler, M., Vögler, A., & Zakharov, V. 2004, ApJL, 607, L59
Krat, V. A., Dul'Kin, L. Z., Validov, M. A., et al. 1974, ATsir, 807, 1
Lagg, A., Solanki, S. K., Doerr, H. P., et al. 2016, A&A, 596, A6
Lagg, A., Solanki, S. K., Riethmüller, T. L., et al. 2010, ApJL, 723, L164
Lites, B. W., Kubo, M., Socas-Navarro, H., et al. 2008, ApJ, 672, 1237
Lites, B. W., Scharmer, G. B., Berger, T. E., & Title, A. M. 2004, SoPh, 221, 65
Martínez González, M. J., Asensio Ramos, A., Manso Sainz, R., et al. 2011, ApJL, 730, L37
Martinez Pillet, V. 1997, in ASP Conf. Ser. 118, Advances in the Physics of Sunspots, ed. B. Schmeider, J. C. del Toro, & M. Vazquez (San Francisco, CA: ASP), 212
Martínez Pillet, V., del Toro Iniesta, J. C., Álvarez-Herrero, A., et al. 2011a, SoPh, 268, 57
Martínez Pillet, V., Del Toro Iniesta, J. C., & Quintero Noda, C. 2011b, A&A, 530, A111
Mehltretter, J. P. 1974, SoPh, 38, 43
Orozco Suárez, D., Bellot Rubio, L. R., del Toro Iniesta, J. C., et al. 2007, ApJL, 670, L61
Parker, E. N. 1979, ApJ, 234, 333
Paxman, R. G., Schulz, T. J., & Fienup, J. R. 1992, J. Opt. Soc. Am., 9, 1072
Paxman, R. G., Seldin, J. J., Loefdahl, M. G., Scharmer, G. B., & Keller, C. U. 1996, ApJ, 466, 1087
Pietarila, A., Hirzberger, J., Zakharov, V., & Solanki, S. K. 2009, A&A, 502, 647
Quintero Noda, C., Shimizu, T., Ruiz Cobo, B., et al. 2016, MNRAS, 460, 1476
Rayleigh, Lord, F. R. S. 1879, PMag, 8, 261
Requerey, I., Del Toro Iniesta, J. C., Bellot Rubio, L. R., et al. 2017a, ApJS, 229, 14
Requerey, I., Ruiz Cobo, B., Del Toro Iniesta, J. C., et al. 2017b, ApJS, 229, 15
Requerey, I. S., Del Toro Iniesta, J. C., Bellot Rubio, L. R., et al. 2014, ApJ, 789, 6
Riethmüller, T. L., Solanki, S. K., Barthol, P., et al. 2017, ApJS, 229, 16
Riethmüller, T. L., Solanki, S. K., Berdyugina, S. V., et al. 2014, A&A, 568, A13
Riethmüller, T. L., Solanki, S. K., Hirzberger, J., et al. 2013a, ApJL, 776, L13
Riethmüller, T. L., Solanki, S. K., & Lagg, A. 2008, ApJL, 678, L157
Riethmüller, T. L., Solanki, S. K., Martínez Pillet, V., et al. 2010, ApJL, 723, L169
Riethmüller, T. L., Solanki, S. K., van Noort, M., & Tiwari, S. K. 2013b, A&A, 554, A53
Scharmer, G. B., Gudiksen, B. V., Kiselman, D., Löfdahl, M. G., & Rouppe van der Voort, L. H. M. 2002, Natur, 420, 151
Scharmer, G. B., Henriques, V. M. J., Kiselman, D., & de la Cruz Rodríguez, J. 2011, Sci, 333, 316
Schüssler, M., & Vögler, A. 2006, ApJL, 641, L73
Smitha, H. N., Anusha, L. S., Solanki, S. K., & Riethmüller, T. L. 2017, ApJS, 229, 17
Socas-Navarro, H., Martínez Pillet, V., Sobotka, M., & Vázquez, M. 2004, ApJ, 614, 448
Solanki, S. K. 1987, PhD Thesis No. 8309, ETH Zürich
Solanki, S. K., Barthol, P., Danilovic, S., et al. 2010, ApJL, 723, L127
Steiner, O., Franz, M., Bello González, N., et al. 2010, ApJL, 723, L180
Tsuneta, S., Ichimoto, K., Katsukawa, Y., et al. 2008, SoPh, 249, 167
van Noort, M., Lagg, A., Tiwari, S. K., & Solanki, S. K. 2013, A&A, 557, A24
van Noort, M., Rouppe van der Voort, L., & Löfdahl, M. G. 2005, SoPh, 228, 191
Wiegelmann, T., Neukirch, T., Nickeler, D. H., et al. 2017, ApJS, 229, 18
Wiegelmann, T., Solanki, S. K., Borrero, J. M., et al. 2010, ApJL, 723, L185
Yelles Chaouche, L., Moreno-Insertis, F., Martínez Pillet, V., et al. 2011, ApJL, 727, L30